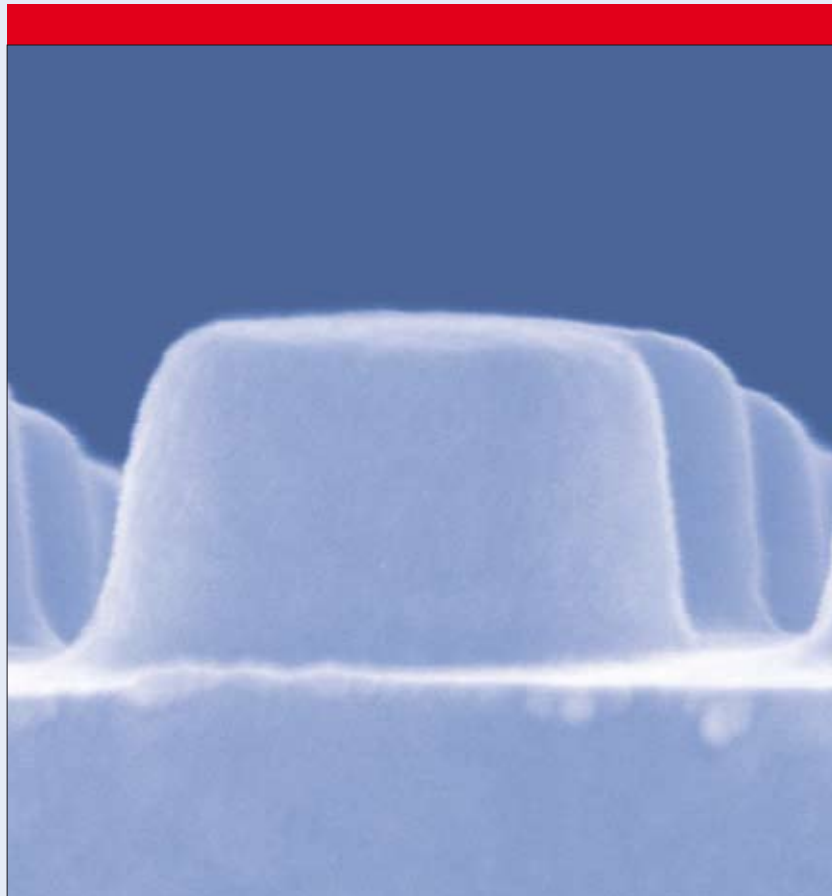


NANOTECHNOLOGY

VOLUME 20 NUMBER 43 28 OCTOBER 2009



www.iop.org/journals/nano

Special issue

Papers celebrating the 20th volume of Nanotechnology
*M Reed, A Engel, M Meyyappan, A Forchel,
D Loss, J Brugger, T Mallouk and M Miles*

Nanopost plasmonic crystals

T T Truong^{1,2,3,6}, J Maria^{1,2,3,6}, J Yao^{1,2,3}, M E Stewart^{1,2,3},
T-W Lee⁴, S K Gray⁵, R G Nuzzo^{1,2,3} and J A Rogers^{1,2,3,7}

¹ Department of Materials Science and Engineering, University of Illinois at Urbana-Champaign, Urbana, IL 61801, USA

² Frederick Seitz Materials Research Laboratory, University of Illinois at Urbana-Champaign, Urbana, IL 61801, USA

³ Department of Chemistry, University of Illinois at Urbana-Champaign, Urbana, IL 61801, USA

⁴ Center for Computation and Technology, Louisiana State University, Baton Rouge, LA 70803, USA

⁵ Chemistry Division and Center for Nanoscale Materials, Argonne National Laboratory, Argonne, IL 60439, USA

E-mail: jrogers@illinois.edu

Received 15 May 2009

Published 2 October 2009

Online at stacks.iop.org/Nano/20/434011

Abstract

We describe a class of plasmonic crystal that consists of square arrays of nanoposts formed by soft nanoimprint lithography. As sensors, these structure show somewhat higher bulk refractive index sensitivity for aqueous solutions in the visible wavelength range as compared to plasmonic crystals consisting of square arrays of nanowells with similar dimensions, with opposite trends for the case of surface bound layers in air. Three-dimensional finite-difference time-domain simulations quantitatively capture the key features and assist in the interpretation of these and related results.

 Supplementary data are available from stacks.iop.org/Nano/20/434011

(Some figures in this article are in colour only in the electronic version)

1. Introduction

Surface plasmon resonance (SPR) sensors based on nanostructured metal films have gained much attention recently, due primarily to their potential to enable label-free biological and chemical detection [1–4]. Such sensors utilize optical excitation of surface plasmons, which provide evanescent electromagnetic surface waves at dielectric-metal boundaries [1, 2, 5, 6]. The properties of these modes can, as a result, be extremely sensitive to changes in the refractive index near the metal surface. The Kretschmann configuration using a prism coupler is the most common setup to excite surface plasmons in flat metal films [1, 2]. Sensors with this design have, however, disadvantages due to their limited throughput, high cost and problems that can arise from wear associated with repeated mechanical contact [1, 7–11]. Recent studies indicate that metal-dielectric interfaces with periodic corrugations provide an alternative coupling strategy that offers the

ability for fabrication by high speed processes such as injection molding and hot embossing [9, 11]. Our own work shows that soft nanoimprint lithographic techniques can yield quasi-three-dimensional (quasi-3D) plasmonic crystals [8, 10] and full three-dimensional (3D) integrated plasmonic crystals [7] based on periodic arrays of cylindrical nanowells embossed in a polymer film that is subsequently coated by blanket deposition of gold layer via electron beam evaporation or sputtering deposition. These structures provide sensors with high sensitivity in quantitative multispectral modes as well as one and two-dimensional (1D and 2D, respectively) imaging capabilities in the near infrared and visible wavelengths, even with broadband, unfiltered light sources such as those associated with a conventional optical microscope [7, 8].

In this paper, we examine a related type of plasmonic crystal that consists of periodic arrays of nanoposts, also formed by soft nanoimprint lithography. We demonstrate that these crystals show enhanced sensitivity to changes in bulk index of refraction in aqueous solution in the visible wavelength range compared to corresponding structures

⁶ These authors contributed equally to this work.

⁷ Author to whom any correspondence should be addressed.

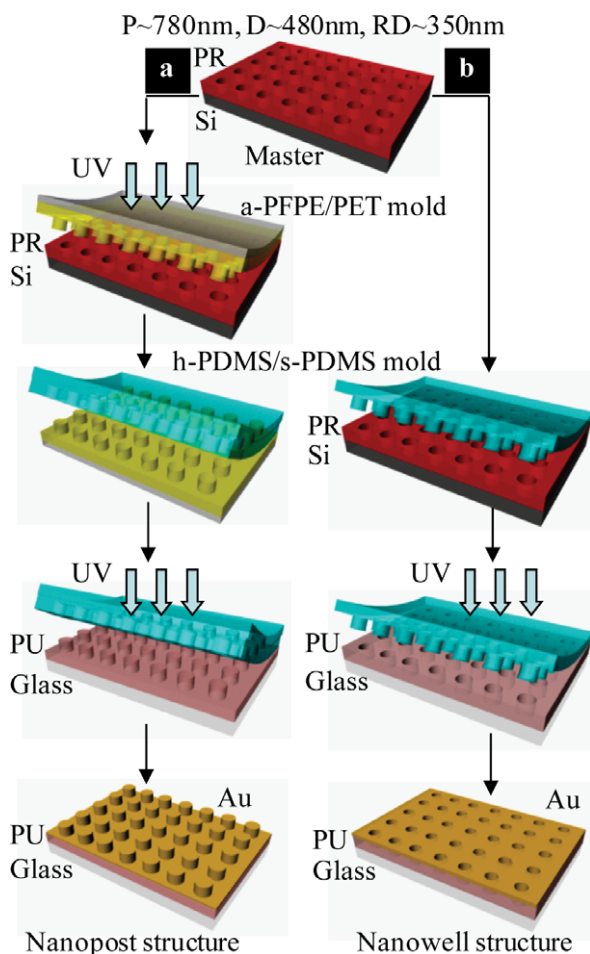


Figure 1. Schematic illustration of the fabrication of nanopost (route (a)) and nanowell (route (b)) plasmonic crystals. The master is composed of photoresist (PR) patterned into a square array of nanowells (diameter $D \sim 480$ nm, periodicity $P \sim 780$ nm and relief depth $RD \sim 350$ nm) on a silicon substrate (Si). Route (a): drop casting acryloxy perfluoropolyether (a-PFPE) and curing under UV light with a poly(ethylene terephthalate) (PET) backing support forms an a-PFPE/PET composite mold. Casting and curing h-PDMS and s-PDMS against the a-PFPE/PET mold forms an h-PDMS/s-PDMS composite mold consisting of nanowells. Molding a UV-curable polyurethane (PU) with this mold generates the PU replica with nanoposts; route (b): casting and curing h-PDMS and s-PDMS against the original master with nanowells forms the h-PDMS/s-PDMS composite mold with nanoposts. Molding PU with this mold under UV light creates a PU replica with nanowells. Deposition of a 35 nm thick layer gold by sputtering completes the fabrication of both the nanopost and nanowell plasmonic crystals.

of nanowells [7]. The opposite behavior is observed for sensitivity to thin film binding events. We use 3D finite-difference time-domain (FDTD) simulations to provide quantitative insights into these and other behaviors.

2. Experiments

2.1. Materials

Unless otherwise specified, reagents were used as received without further purification. Poly(dimethylsiloxane) (soft

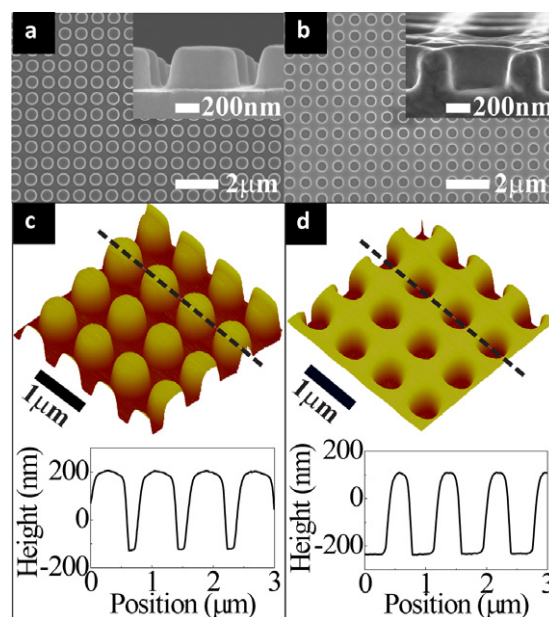


Figure 2. Scanning electron microscope (SEM) ((a) and (b)) and atomic force microscope (AFM) images ((c) and (d)) of the nanopost ((a) and (c)) and nanowell ((b) and (d)) plasmonic crystals. The insets in (a) and (b) show high magnification SEM images of the cross-section views. The nanopost sample shows posts with a diameter of 520 nm and a periodicity of 736 nm, while the nanowell sample shows wells with a diameter of 480 nm and a periodicity of 760 nm. The graphs in (c) and (d) show the height analysis across an array of nanoposts (c) and nanowell (d). The relief depths for the nanoposts and nanowells are shown to be 325 nm and 340 nm, respectively.

PDMS, Sylgard 184, Dow Corning) was purchased from Ellsworth Adhesives. Components for hard PDMS, including (25–30% methylhydrosiloxane)-(dimethylsiloxane) copolymer (HMS-301), (7–8% vinylmethylsiloxane)-(dimethylsiloxane) copolymer (VDT-731), platinum-divinyltetramethyldisiloxane complex in xylene (SIP6831.2) and (1,3,5,7-tetravinyl-1,3,5,7-tetramethylcyclotetrasiloxane) (SIT7900.0), were purchased from Gelest. Fluorinated acrylate oligomer (CN4000, MW = 1000 g mol⁻¹) was purchased from Sartomer Company. Photoinitiator Darocur 4265, which contains 50% of 2,4,6-trimethylbenzoyl-diphenyl-phosphineoxide and 50% of 2-hydroxy-2-methyl-1-phenyl-propanone, was purchased from Ciba Specialty Chemicals. Photocurable polyurethane (PU, NOA 73) was purchased from Norland Products. Poly(ethylene glycol) solutions (1.4–5.6%) were prepared with deionized (DI) water (18 MΩ) generated using Millipore Milli-Q Academic A-10 system.

2.2. Fabrication of plasmonic crystals

Figure 1 schematically illustrates the fabrication processes for both the nanopost (route (a)) and nanowell (route (b)) 3D plasmonic crystals. Both cases start with a pattern of photoresist (i.e. ‘master’) on a SiO₂/Si substrate, in the geometry of a square array of cylindrical nanowells with diameters of ~ 480 nm and relief depths of ~ 350 nm, and a periodicity of ~ 780 nm. The nanopost fabrication requires

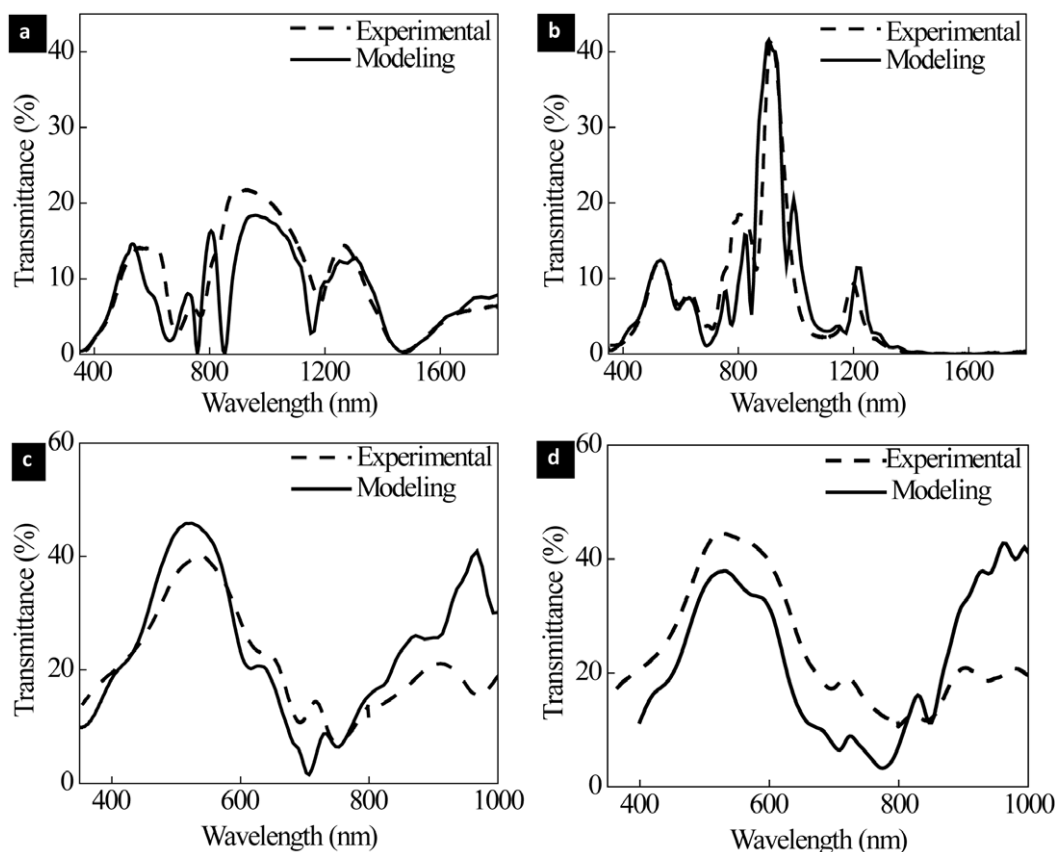


Figure 3. Experimental (dashed line) and modeling results (solid line) for normal incidence transmission spectra in air ((a) and (b)) and water ((c) and (d)) for nanopost ((a) and (c)) and nanowell ((b) and (d)) 3D plasmonic crystals. The calculated spectra were generated from quantitative electrodynamics modeling. For the nanopost sample a periodicity of 736 nm, a diameter of 520 nm, a relief depth of 324 nm and a thicknesses of gold of 32 nm on top, 20 nm on bottom and 10 nm on the post sidewall were used in the modeling while for the nanowell sample a periodicity of 760 nm, a diameter of 480 nm, a relief depth of 340 nm and a thicknesses of gold of 36 nm on top, 20 nm on the bottom and 12 nm on the sidewall were considered.

three consecutive molding steps and uses previously reported drop casting and photocuring procedures [12] to form an acryloxy perfluoropolyether (a-PFPE, CN4000) mold with a poly(ethyleneterephthalate) (PET) film as a backing support. As reported previously, a-PFPE, due to its low surface energy, relatively high Young's modulus and good chemical resistance, enables high resolution patterning in various soft lithographic processes without the need of fluorination treatment required for more widely used materials such as poly(dimethylsiloxane) [12]. This a-PFPE/PET mold was used in a second molding step to make a hard PDMS (h-PDMS)/soft PDMS (s-PDMS) composite mold that replicates the original nanowell array structure of the master. In particular, the process includes spin casting and thermally curing at 65 °C for 2 min a thin layer of h-PDMS (~20 μm thick) prepolymer with a thicker layer of s-PDMS (~4 mm thick) as a backing support against the surface of the a-PFPE/PET mold [12, 13]. The third molding step involved drop casting and photocuring of polyurethane (NOA 73) on glass [10] against the h-PDMS/s-PDMS mold to produce a reverse replica of the master, i.e. a structure of square arrays of cylindrical nanoposts.

The fabrication process for the nanowell plasmonic crystal consists of two molding steps. The first step began with the preparation of the h-PDMS/s-PDMS composite mold directly

from patterned PR on a SiO_2/Si substrate. The resulting h-PDMS/s-PDMS composite mold, which consisted of a square array of cylindrical nanoposts, was used in a second molding step to emboss a square array of nanowells on a layer of NOA.

Blanket deposition of a layer of gold (~35 nm thick) by sputtering (ATC 2000 custom four gun co-sputtering system, AJA International) in 5 mTorr of Argon on the molded layers of NOA completed the fabrication of both the nanopost and nanowell plasmonic crystals.

2.3. Transmission-mode spectrophotometry

Transmission spectra of both types of plasmonic crystals were measured with a Varian 5G UV-vis-NIR spectrophotometer operating in normal incidence transmission mode. Injection of solutions of poly(ethylene glycol) with different concentrations (0–5.6 wt%) into a flow cell of PDMS built around the plasmonic crystals [8] using a syringe pump at the rate of 0.1 ml min^{-1} led to changes in refractive index surrounding the plasmonic crystals. Transmission measurements collected during this process revealed the multispectral plasmonic response of both types of crystals to changes in bulk, surrounding index of refraction.

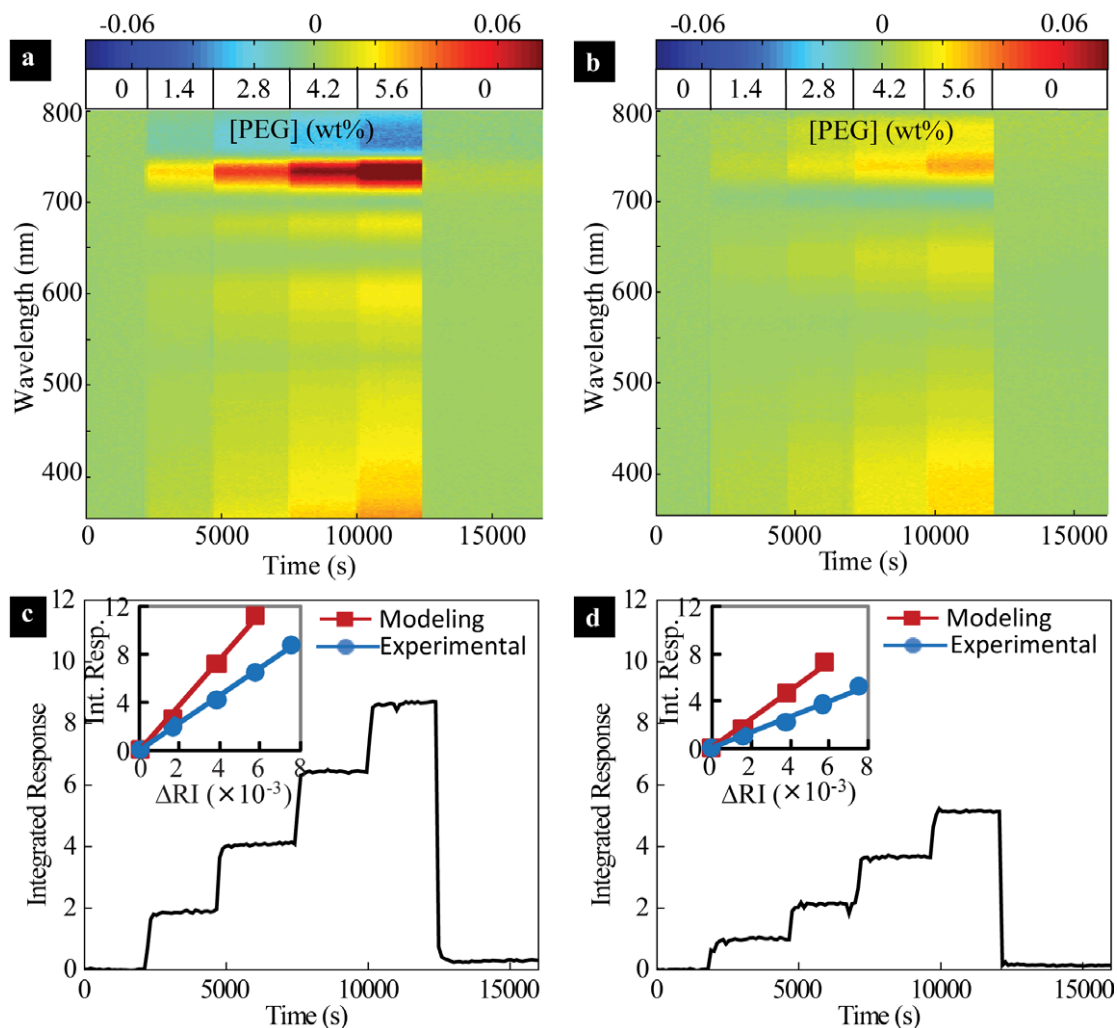


Figure 4. Multispectral plasmonic response in the wavelength range of 355–800 nm of a nanostrip plasmonic crystal ((a) and (c)) and of a nanowell plasmonic crystal ((b) and (d)) to sequential injections of increasing concentrations of aqueous polyethylene glycol (PEG) solutions. ((a) and (b)) color contour plots of the change in transmission (T) as a function of wavelength and time with the corresponding injected PEG concentrations. ((c) and (d)) integrated response as a function of time over 355–800 nm. The insets show the linear correlation between the integrated responses and the changes in refractive index of the PEG solutions. The red and blue lines show experimental and modeling results, respectively.

2.4. Microfluidic patterning of plasmonic crystals

Single channel microfluidic devices with channel widths of $\sim 80 \mu\text{m}$ were formed by casting and curing PDMS against a pattern of photoresist on a silicon wafer. Pieces of PDMS formed in this manner were placed into conformal contact with the plasmonic crystals. While in contact, the resulting microfluidic channels were filled with a 0.17 mg ml^{-1} solution of fibrinogen in phosphate buffered saline (PBS) using the channel outgas technique [14]. After incubating for 1 h, the channels were rinsed with buffer and the PDMS elements were removed. The crystals were then sequentially rinsed with PBS and water and dried under a stream of nitrogen.

2.5. Two-dimensional spatial imaging of protein patterned plasmonic crystals

Transmission mode images of the crystals with patterns of protein formed according to the procedures described above were acquired using an AX-70 upright microscope (Olympus)

equipped a Magnafire CCD (Optronics) that has an 1280×1024 array of imaging pixels, each of which is $6.7 \mu\text{m} \times 6.7 \mu\text{m}$. The sample was illuminated with white light at normal incidence and the zero-order transmitted light was collected with a $20\times$ objective and projected onto the CCD. Considering the collection optics, the resolution of this imaging system is $\sim 2 \mu\text{m}$. The raw images had smooth variations in brightness as a function of distance from the center of the image. This uneven illumination was removed by background correction.

2.6. Finite difference time-domain (FDTD) calculations

The FDTD method was used to model the transmission spectra and electromagnetic field distributions [15, 16] of both types of plasmonic crystal. The post and well arrays were defined in a gold film parallel to the x - y plane, with air or water on the top side and polymer on the bottom side. Periodic boundary conditions were applied at the edges of the x - y plane (for all z) and perfectly matching layers were

used in the upper and lower z grid boundaries to absorb waves exiting the simulation box. The total field/scattered field method [15] was used to inject a linearly polarized, broad band light pulse into the system propagating along z from the top side toward the bottom side of the gold film. A Drude plus two-pole Lorentzian model for the complex, frequency-dependent gold permittivity was employed [17], with parameters fit to empirical dielectric constant data. Details of the implementation can be found elsewhere [18]. The frequency-resolved electric and magnetic fields were obtained with time-to-frequency Fourier transforms. The normal of the corresponding Poynting or flux vector was integrated across the x - y -plane in the polymer region to obtain the transmission spectra. The calculations involved evenly spaced grids in x , y and z with grid spacings of 4 nm. The nanopost calculations involved $N_x \times N_y \times N_z = 184 \times 184 \times 750$ total grid points and the nanowell ones involved $190 \times 190 \times 750$ total grid points. Propagations were carried out for 150 fs.

3. Results and discussion

Figures 2(a) and (b) show scanning electron micrographs (SEM) of the nanopost and nanowell plasmonic crystals, respectively. The high magnification SEM images in the insets show the cross sections of the embossed polymeric nanoposts and nanowells and their respective diameters. Although both structures were fabricated from a single master, their feature sizes are slightly different: the nanopost plasmonic crystal has cylindrical posts with diameters of 520 nm and periodicities of 736 nm whereas the nanowell one has cylindrical wells with diameters of 480 nm and periodicities of 760 nm. Different levels of shrinkage associated with the different fabrication steps can account for these observations [12]. Atomic force microscopy (AFM) images in the top frames of figures 2(c) and (d) provide additional views of the geometries of the nanopost and nanowell structures. The linecuts in the bottom frames reveal heights of 325 nm and 340 nm for the nanoposts and nanowells, respectively.

To evaluate the optical properties, we measured and calculated the zero-order, normal incidence transmission spectra in both air and water. The results appear as dashed and solid lines, respectively, in the graphs of figure 3. Figures 3(a) and (b) show transmission spectra for nanopost and nanowell crystals in air. Figures 3(c) and (d) correspond to transmission spectra for those crystals in water. In the case of the nanoposts, good agreement between experiment and calculation was obtained by using a 32 nm gold layer for the nanopost top with 10 nm sidewalls, and a 20 nm gold layer for the bottom film. For the nanowells, we used a 36 nm gold layer for the top film, and a 20 nm gold layer for the nanowell bottom with 12 nm sidewalls. All of these thickness values are within uncertainties of those measured directly by transmission electron microscopy (TEM) (see supporting information (figure S1 available at stacks.iop.org/Nano/20/434011) and [1]). Diagrams of the structures used for modeling appear in the supporting information (figure S2 available at stacks.iop.org/Nano/20/434011).

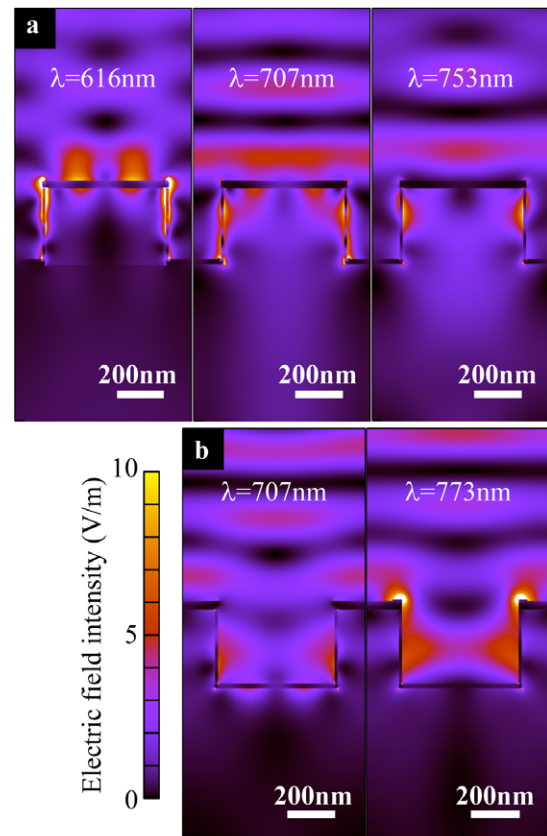


Figure 5. (a) Calculated electric field intensities, $|E_z|^2$, for the nanopost plasmonic crystal in an aqueous solution associated with the resonances in transmission at wavelengths ~ 616 , ~ 707 , and ~ 753 nm; (b) calculated electric field intensities, $|E_z|^2$, for the nanowell plasmonic crystals in an aqueous solution associated with the resonances in transmission at the wavelengths ~ 707 and ~ 773 nm.

The bulk refractive index sensitivity of both of these crystals was measured by sequentially injecting aqueous solutions of poly(ethylene glycol) (PEG, $M = 10000$) with increasing concentrations (0–5.6 wt%) over the crystals through a fluid flow cell as described previously [7, 8, 19]. For a given temperature there is a linear relation between the wt% and the solution's refractive index (RI). At 298 K, 0 wt% (pure water) corresponds to an RI of 1.332 and 5.6 wt% corresponds to an RI of 1.340. Transmission spectra collected over time show changes in peak positions and intensities as the refractive index of the solution is increased. The series of difference spectra were then referenced and normalized to the spectrum at time $t = 0$. Figures 4(a) and (b) show the normalized changes in transmission in visible range (355–800 nm) as solutions of increasing PEG concentration were passed through the nanopost and nanowell plasmonic crystals, respectively. The nanopost structure (made from the same master) exhibits the greater sensitivity, particularly in the 700–800 nm wavelength range. The integrated response over a band of wavelengths is calculated by

$$R = \int \frac{|\Delta(\%T(\lambda))|}{T_{\text{baseline}}} d\lambda = \int \frac{|T_{\text{solution}} - T_{\text{baseline}}|}{T_{\text{baseline}}} d\lambda \quad (1)$$

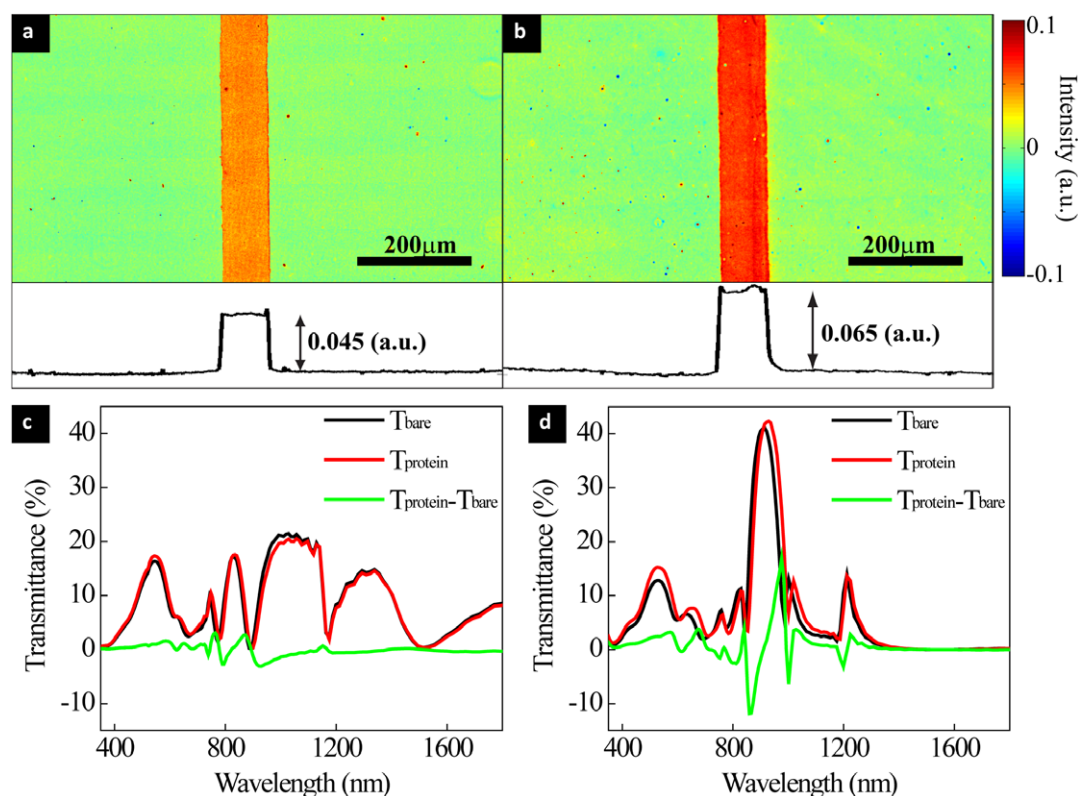


Figure 6. Transmitted-light images of a protein, fibrinogen, nonspecifically adsorbed to the surfaces of nanopost (a) and nanowell (b) plasmonic crystals. The bottom curves show the measured light intensity contrast from the protein regions. The nanopost crystal has a periodicity of 745 nm, a nanopost diameter of 545 nm and a nanopost relief depth of 345 nm while the nanowell crystal has a periodicity of 765 nm, a nanowell diameter of 560 nm and a nanowell relief depth of 320 nm. Frames (c) and (d) show the calculated normal incidence transmission spectra in air without protein (black curves), with a thin layer of protein (~ 10 nm) (red curves) and the spectral difference (green curves) for the nanopost and nanowell plasmonic crystals described in figure 3.

where T_{solution} is the observed transmission in a given solution and T_{baseline} is the transmission in pure solvent, i.e. water [19]. Figures 4(c) and (d) show the responses computed by integrating the data of figures 4(a) and (b) over the entire wavelength range. This integrated response depends linearly on changes in the refractive index of the PEG solutions as shown in the figures 4(c) and (d) insets. We define the sensitivity to be the slope of the response versus refractive index change curve. The measured sensitivities are 1100 ± 100 nm/RIU (RIU defined as refractive index unit) and 660 ± 60 nm/RIU for the nanopost and nanowell cases, respectively. This result corresponds to an increased sensitivity of $\sim 70\%$ for the nanopost crystal. The red curves in the insets of figures 4(c) and (d) correspond to the calculated integrated responses and lead to sensitivities of ~ 1900 nm/RIU and ~ 1200 nm/RIU for the nanopost and nanowell cases, respectively. While these sensitivities are somewhat larger than the experimental ones, they confirm that the nanopost crystals are more sensitive than the nanowell ones in the case of bulk solutions with refractive indices near the water's refractive index.

The structured transmission spectra in figures 3(a)–(d) arise due to a variety of plasmonic effects, as discussed in previous work [1, 5, 8, 15]. The broad spectral feature in the 400–600 nm range is the characteristic transmission associated with a thin gold film. The structures at longer wavelengths are

due to a variety of plasmonic and diffractive features. These features include localized surface plasmons (LSPs) associated with the component nanoposts or nanowells. Superimposed on broad LSP resonances, or possibly isolated from them, can be features that depend strongly on the periodicities of the structures: Bloch wave surface plasmon polaritons (BW-SPPs) and diffractive Wood (or Rayleigh) anomalies (WAs). Simple formulae [15] can be used to predict the positions of these periodic features, but there can be overlapping and coupling of, e.g., LSPs and BW-SPPs, which can complicate clear assignments. Time-to-frequency Fourier transforms of the electric field from our FDTD calculations at specific frequencies (or wavelengths) of interest provide insights into the nature of the electromagnetic near-fields, as illustrated in figure 5. The z -component of the electric field, E_z , is interesting because it can only arise from scattering or plasmonic effects since the incident light is polarized along a transverse direction (x). Figure 5(a) shows the calculated $|E_z|^2$ at the wavelengths of 616, 707 and 753 nm for the nanopost plasmonic crystal while figure 5(b) shows the calculated $|E_z|^2$ at the wavelengths of 707 and 773 nm for the nanowell crystal. (See figures S3 and S4 of the supporting information available at stacks.iop.org/Nano/20/434011 for 3D intensity images.) The wavelengths employed are those associated with minima in the transmission spectra which often correlate with regions of strong absorption by the crystal. These plots show

that the three transmission minima exhibited by the nanopost structure and the two transmission minima exhibited by the nanowell structure have strong LSP contributions at the top and bottom rims of the nanopost and nanowell, respectively. By comparing the intensity of the electromagnetic fields, we see that the nanopost structure exhibits stronger LSPs than the nanowell structure for most of the computed wavelengths. This fact in combination with the extra peak presented by the nanopost plasmonic crystal accounts, at least partly, for the increase in sensitivity in the visible range for this type of crystal.

The increase in the bulk refractive index sensitivity at visible wavelengths for nanopost plasmonic crystals suggests an expected enhancement in monitoring surface binding events using an optical microscope, as reported previously [7, 8]. Transmission mode imaging of a patterned, nonspecifically adsorbed protein, shown in figures 6(a) and (b), was conducted to explore this possibility. The results show that the nanopost crystals have somewhat smaller contrast than nanowell crystals (~ 0.045 (au) for nanoposts versus ~ 0.065 (au) for nanowells). Note that in this experiment we have air (not water) above the protein layer. The effective refractive indices that result from a thin protein layer (RI = 1.65) and a semi-infinite air layer (RI = 1) are unlikely to be close to that of water (RI = 1.33) and so different plasmonic resonances are likely playing a role in this case; their spatial extent of overlap between these resonances and the 'analyte' is also different. To confirm the imaging data, a thin layer of protein (10 nm) with a refractive index of 1.65 was used in FDTD calculations. Figures 6(c) and (d) show the calculated normal incidence transmission spectra of nanopost and nanowell crystals with and without protein films and the difference between those spectra. The changes in transmission within the visible range (355–800 nm) shown in the green curves are smaller in the case of nanopost than nanowell crystals. Calculations carried out by slightly varying the protein's layer RI allow us to estimate a sensitivity of ~ 2400 nm/RIU for nanopost crystals and a sensitivity of ~ 4400 nm/RIU for nanowell crystals. These results are thus consistent with the experimental imaging measurements in air.

Finally, to explore the degree to which different optical properties of the nanopost and nanowell plasmonic crystals are due to different overall geometry (i.e. nanopost versus nanowell), compared to differences in corresponding dimensions discussed previously or to variations in the thickness of the gold, we spin cast a layer of polyurethane on top of the embossed side of both plasmonic crystals and cured it under UV light. This process yielded two samples with the same nominal geometry, as represented in the schematic illustration at the bottom of figure 7. Since the plasmonic crystals are fabricated from the same master they should, in principle, be symmetric, because the conformal gold layer in both samples is surrounded on both sides by NOA. Figure 7(a) shows that the experimental transmission spectra of nanopost and nanowell plasmonic crystals in cured polyurethane are qualitatively similar, but with some notable differences, most likely due to differences in feature sizes and gold thicknesses resulting from the molding and deposition processes. Calculated transmission spectra shown

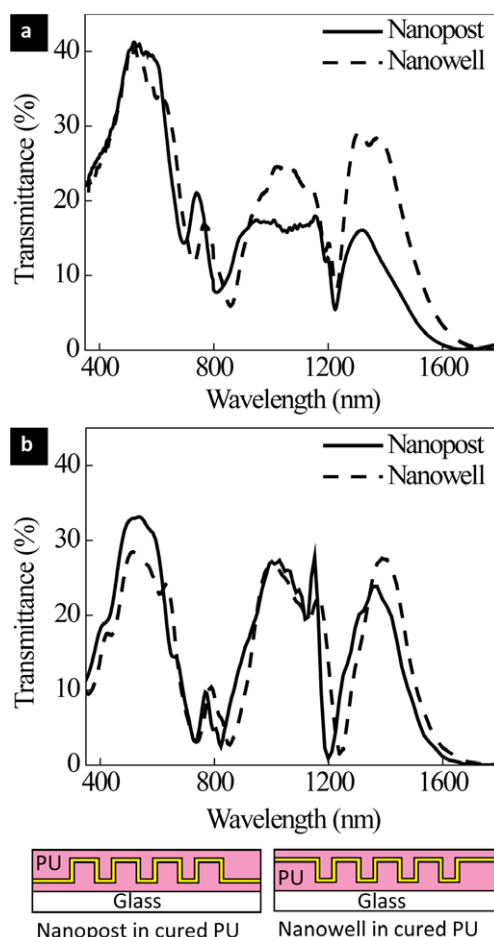


Figure 7. Comparison of the transmission spectra of 'similar configurations' of nanopost and nanowell plasmonic crystals with cured polyurethane (PU) on top. Frame (a) shows the experimental data while frame (b) shows the calculated data. Both of the samples were prepared by spin coating and UV curing a thin layer of polyurethane (PU, NOA-73) on top of the nanopost and nanowell plasmonic crystals. The geometry of the samples is shown in the bottom diagrams.

in figure 7(b) confirm behaviors similar to those of the experimental data.

4. Summary and conclusion

In summary, we have described a class of plasmonic crystal containing square arrays of nanometer scale posts and used finite-difference time-domain (FDTD) calculations to model the optical properties. The experimental and modeling data confirm an increase in bulk refractive index sensitivity for aqueous solutions in the visible wavelengths of $\sim 70\%$ for these crystals compared to similar structures that consist of square arrays of nanowells. Opposite trends are observed for thin film binding events in air. The results suggest that nanopost and nanowell crystals might offer complementary advantages in biosensing and imaging with visible light.

Acknowledgments

This work was carried out in part at the Frederick Seitz Materials Research Laboratory Central Facilities, University

of Illinois, which are partially supported by the US Department of Energy under grants DE-FG02-07ER46453 and DE-FG02-07ER46471. It was also supported by NSF through grants DMI 03-55532 and the Center for Nanoscale Chemical Electrical Mechanical Manufacturing Systems at the University of Illinois, which was funded by National Science Foundation under grant DMI-0328162. The work at Argonne National Laboratory was supported by the Office of Basic Energy Sciences, Division of Chemical Sciences, Geosciences, and Biosciences, US Department of Energy (DE-AC02-06CH11357). The authors gratefully acknowledge the use of the *Turing* cluster maintained and operated by the Computational Science and Engineering Program at the University of Illinois. *Turing* is a 1536-processor Apple G5 X-server cluster devoted to high performance computing in engineering and science. This work was also funded in part by a grant from the Vietnam Education Foundation (VEF). The opinions, findings, and conclusions stated herein are those of the authors and do not necessarily reflect those of VEF.

References

- [1] Homola J 2008 Surface plasmon resonance sensors for detection of chemical and biological species *Chem. Rev.* **108** 462–93
- [2] Homola J 2003 Present and future of surface plasmon resonance biosensors *Anal. Bioanal. Chem.* **377** 528–39
- [3] Abdulhalim I, Zourob M and Lakhtakia A 2008 Surface plasmon resonance for biosensing: a mini-review *Electromagnetics* **28** 214–42
- [4] Stewart M E, Anderton C R, Thompson L B, Maria J, Gray S K, Rogers J A and Nuzzo R G 2008 Nanostructured plasmonic sensors *Chem. Rev.* **108** 494–521
- [5] Pitarke J M, Silkin V M, Chulkov E V and Echenique P M 2007 Theory of surface plasmons and surface-plasmon polaritons *Rep. Prog. Phys.* **70** 1–87
- [6] Maier S A 2007 *Plasmonics: Fundamentals and Applications* (New York, NY: Springer)
- [7] Yao J, Stewart M E, Maria J, Lee T W, Gray S K, Rogers J A and Nuzzo R G 2008 Seeing molecules by eye: surface plasmon resonance imaging at visible wavelengths with high spatial resolution and submonolayer sensitivity *Angew. Chem. Int. Edn* **47** 5013–7
- [8] Stewart M E, Mack N H, Malyarchuk V, Soares J A N T, Lee T-W, Gray S K, Nuzzo R G and Rogers J A 2006 Quantitative multispectral biosensing and 1D imaging using quasi-3D plasmonic crystals *Proc. Natl Acad. Sci. USA* **103** 17143–8
- [9] Thirstrup C, Zong W, Borre M, Neff H, Pedersen H C and Holzhuetter G 2004 Diffractive optical coupling element for surface plasmon resonance sensors *Sensors Actuators B* **100** 298–308
- [10] Malyarchuk V, Hua F, Mack N, Velasquez V, White J, Nuzzo R G and Rogers J A 2005 High performance plasmonic crystal sensor formed by soft nanoimprint lithography *Opt. Express* **13** 5669–75
- [11] Dostálek J, Homola J and Miler M 2005 Rich information format surface plasmon resonance biosensor based on array of diffraction gratings *Sensors Actuators B* **107** 154–61
- [12] Truong T T, Lin R, Jeon S, Lee H H, Maria J, Gaur A, Hua F, Meinel I and Rogers J A 2007 Soft lithography using acryloxy perfluoropolyether composite stamps *Langmuir* **23** 2898–905
- [13] Hua F *et al* 2004 Polymer imprint lithography with molecular-scale resolution *Nano Lett.* **4** 2467–71
- [14] Monahan J, Gewirth A A and Nuzzo R G 2001 A method for filling complex polymeric microfluidic devices and arrays *Anal. Chem.* **73** 3193–7
- [15] Taflove A and Hagness S C 2005 *Computational Electrodynamics: The Finite-Difference Time-Domain Method* (Norwood, MA: Artech House Publishers)
- [16] Chang S-H, Gray S and Schatz G 2005 Surface plasmon generation and light transmission by isolated nanoholes and arrays of nanoholes in thin metal films *Opt. Express* **13** 3150–65
- [17] Gray S K and Kupka T 2003 Propagation of light in metallic nanowire arrays: finite-difference time-domain studies of silver cylinders *Phys. Rev. B* **68** 045415
- [18] Lee T W and Gray S K 2005 Subwavelength light bending by metal slit structures *Opt. Express* **13** 9652–9
- [19] Maria J, Truong T T, Yao J, Lee T-W, Nuzzo R G, Leyffer S, Gray S K and Rogers J A 2009 Optimization of 3D plasmonic crystal structures for refractive index sensing *J. Phys. Chem. C* **113** 10493–9

Supporting Information

Nanopost Plasmonic Crystals

T T Truong^{1,4}, **J Maria**^{1,4}, **J Yao**¹, **M E Stewart**¹, **T-W Lee**², **S K Gray**³, **R G Nuzzo**¹ and **J A Rogers**^{1,5}

¹Department of Materials Science and Engineering, Frederick Seitz Materials Research Laboratory and Department of Chemistry, University of Illinois at Urbana-Champaign, Urbana, IL 61801

²Chemistry Division and Center for Nanoscale Materials, Argonne National Laboratory, Argonne, IL 60439

³Center for Computation & Technology, Louisiana State University, Baton Rouge, LA 70803

⁴These authors contributed equally to this work.

⁵To whom correspondence should be addressed. Email: jrogers@illinois.edu

Figure S1: Transmission electron micrographs (TEM) of the cross section of a nanopost plasmonic crystal. The top frame shows a typical cross section. The lower frames present high magnification TEM images showing the thickness of the sputtered gold on (a) the top of the crystal (~35nm), (b) the sidewall (~10-14nm) and (c) the bottom of the nanoposts (~25nm).

Figure S2: Schematic diagram of the unit cell cross section used in the FDTD modeling of (a) a nanopost plasmonic crystal and (b) a nanowell plasmonic crystal. The nanopost crystal has a periodicity of 736nm, with a nanopost diameter of 520nm and nanopost depth of 325nm. Gold thicknesses of 32nm on the top, 20nm on the sidewall and 10nm on the bottom of the nanopost were used for the modeling. The nanowell crystal has a periodicity of 760nm, with a nanowell diameter of 480nm and nanowell depth of 340nm. The thicknesses of gold on the nanowell top, bottom and sidewall were 36nm, 20nm and 12nm, respectively. The refractive indexes of the polymer, air and water are 1.56, 1.00 and 1.33, respectively.

Figure S3: Three-dimensional images of the computed electromagnetic field intensities for the polymer/nanopost/water system associated with the resonances in transmission at (a) 616nm, (b) 707nm, and (c) 753nm.

Figure S4: Three-dimensional images of the computed electromagnetic field intensities for the polymer/nanowell/water system associated with the resonances in transmission at (a) 707nm, and (b) 773nm.

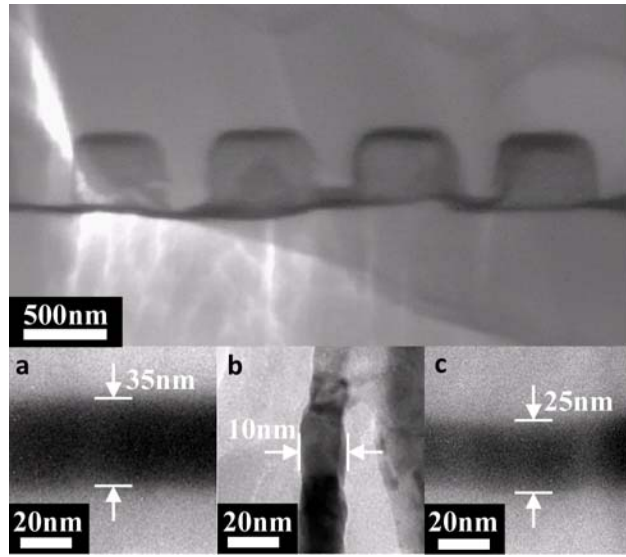


Figure S1

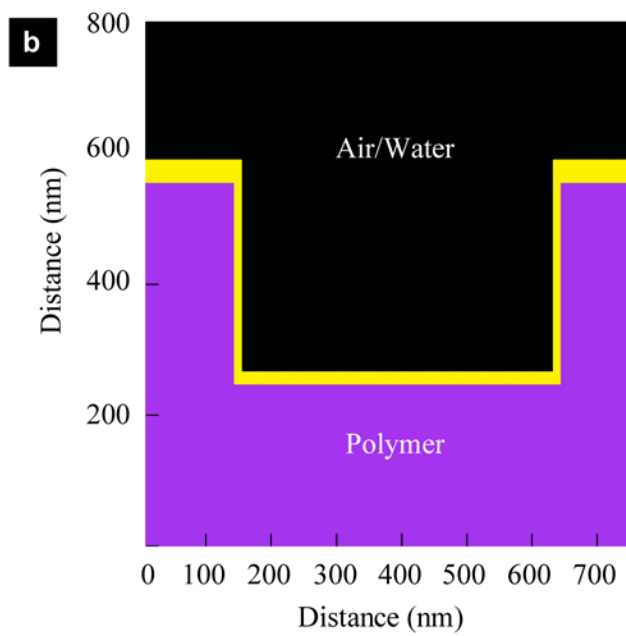
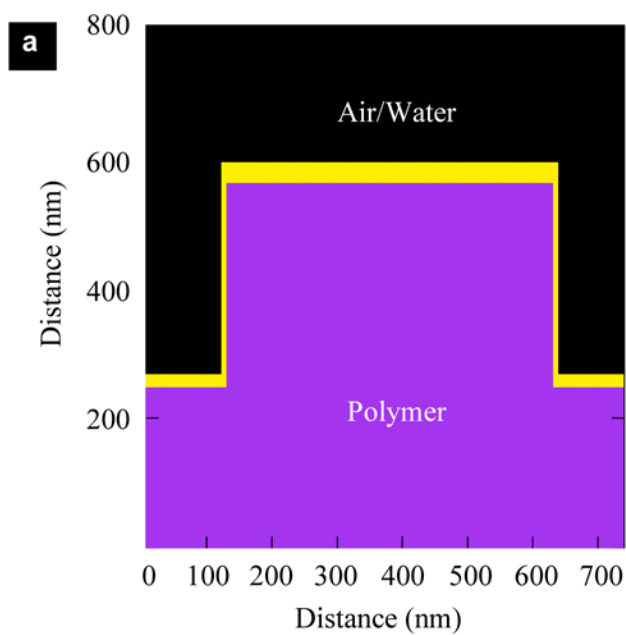


Figure S2

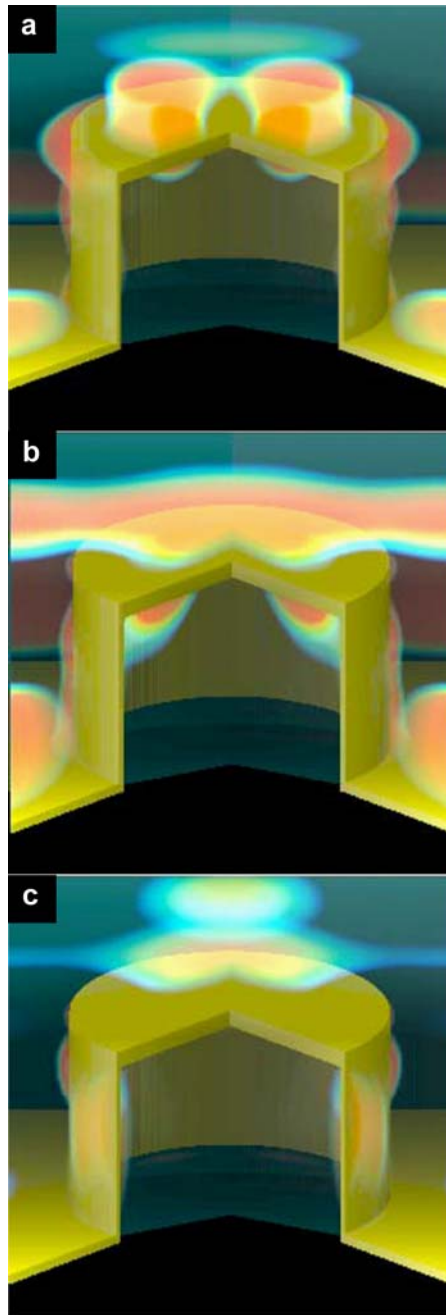


Figure S3

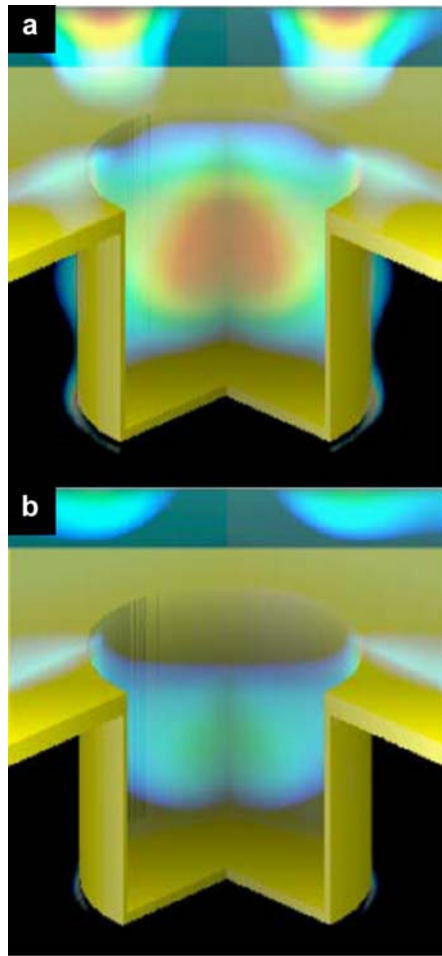


Figure S4